Original

Liang, J.-H.; Deutsch, C.; McWilliams, J.C.; Baschek, B.; Sullivan, P.P.; Chiba, D.:

Parameterizing bubble-mediated air-sea gas exchange and its effect on ocean ventilation

In: Global Biogeochemical Cycles (2013) AGU

DOI: 10.1002/gbc.20080

GLOBAL BIOGEOCHEMICAL CYCLES, VOL. 27, 894–905, doi:10.1002/gbc.20080, 2013

Parameterizing bubble-mediated air-sea gas exchange and its effect on ocean ventilation

Jun-Hong Liang,[1,2] Curtis Deutsch,[1] James C. McWilliams,[1] Burkard Baschek,[3] Peter P. Sullivan,[4] and David Chiba[1]

Received 11 October 2012; revised 21 May 2013; accepted 6 August 2013; published 30 August 2013.

[1] Bubbles play an important role in the exchange of gases between the atmosphere and ocean, altering both the rate of exchange and the equilibrium gas saturation state. We develop a parameterization of bubble-mediated gas fluxes for use in Earth system models. The parameterization is derived from a mechanistic model of the oceanic boundary layer that simulates turbulent flows and the size spectrum of bubbles across a range of wind speeds and is compared against other published formulations. Bubble-induced surface supersaturation increases rapidly with wind speed and is inversely related to temperature at a given wind speed, making the effect of bubbles greatest in regions that ventilate the deep ocean. The bubble-induced supersaturation in high-latitude surface waters compensates a substantial fraction of the undersaturation caused by surface cooling. Using a global ocean transport model, we show that this parameterization reproduces observed saturation rate profiles of the noble gas Argon in the deep Atlantic and Pacific Oceans. The abyssal argon supersaturation caused by bubbles varies according to gas solubility, ranging from $\sim 0.7\%$ for soluble gases like CO_2 to $\sim 1.7\%$ for less soluble gases such as N_2. Bubble-induced supersaturation may be significant for biologically active gases such as oxygen.

Citation: Liang, J.-H., C. Deutsch, J. C. McWilliams, B. Baschek, P. P. Sullivan, and D. Chiba (2013), Parameterizing bubble-mediated air-sea gas exchange and its effect on ocean ventilation, *Global Biogeochem. Cycles*, *27*, 894–905, doi:10.1002/gbc.20080.

1. Introduction

[2] Oceanic-dissolved gas concentrations are governed by biogeochemical processes, such as phytosynthesis/respiration that produce/consume dissolved gases [e.g., *Sarmiento and Gruber*, 2006] and by physical processes including gas transfer at the ocean surface, heating/cooling, bubbles [*Keeling*, 1993], and mixing [e.g., *Ito and Deutsch*, 2006]. Oceanic distributions of different gases have been used to quantify different physical and biogeochemical processes in the ocean. A few examples are the diagnosis of diapycnal mixing rate using argon (Ar) saturation levels [*Ito and Deutsch*, 2006; *Ito et al.*, 2007], the quantification of respiration rate using dissolved oxygen (O_2) concentrations [*Jenkins*, 1982], and the determination of coastal bottom water and the deep ocean ventilation at high latitudes [e.g., *Baschek*, 2003; *Nicholson et al.*, 2010]. Among the physical processes, the effect of bubbles is least understood and is most poorly quantified. Bubbles are entrained into the ocean during the breaking of surface gravity waves. They move under the action of boundary layer turbulence, rise by buoyancy, exchange gases with surrounding water, and change size due to the change of both gas amount and ambient pressure. Small bubbles, with slow buoyant rising velocities, are trapped in the boundary layer and dissolve completely. Large bubbles, with rapid buoyant rising velocities, are able to rise despite the downward turbulent motions and eventually burst at the ocean surface. As bubbles are compressed by hydrostatic pressure and surface tension, gases inside can be squeezed into the ocean even when it is supersaturated with respect to the atmosphere, causing gases to diffuse from the ocean to the atmosphere through the air-sea interface. Consequently, there is a gas supersaturation state, at which the gas flux through all bubbles are into the ocean, and this gas flux balances the diffusive gas flux from the ocean to the atmosphere through ocean surface (see top panel of Figure 1).

[3] Recent studies have shown that near-surface bubbles play an important role in the ocean-atmosphere exchange of gases at moderate to high wind speeds when bubbles are abundant [e.g., *Hamme and Emerson*, 2002, 2006; *D'Asaro and McNeil*, 2007; *Stanley et al.*, 2009; *Vlahos and Monahan*, 2009; *Vagle et al.*, 2010]. Bubbles influence

[1]Department of Atmospheric and Oceanic Sciences, University of California, Los Angeles, California, USA.
[2]Applied Physics Laboratory, University of Washington, Seattle, Washington, USA.
[3]Institute of Coastal Research, Helmholtz-Zentrum Geesthacht Centre, Geesthacht, Germany.
[4]Mesoscale and Microscale Meteorology Division, National Center for Atmospheric Research, Boulder, Colorado, USA.

Corresponding author: J.-H. Liang, Applied Physics Laboratory, University of Washington, 1013 NE 40th Street, Seattle, WA 98105, USA. (liangjh@apl.uw.edu)

0886-6236/13/10.1002/gbc.20080

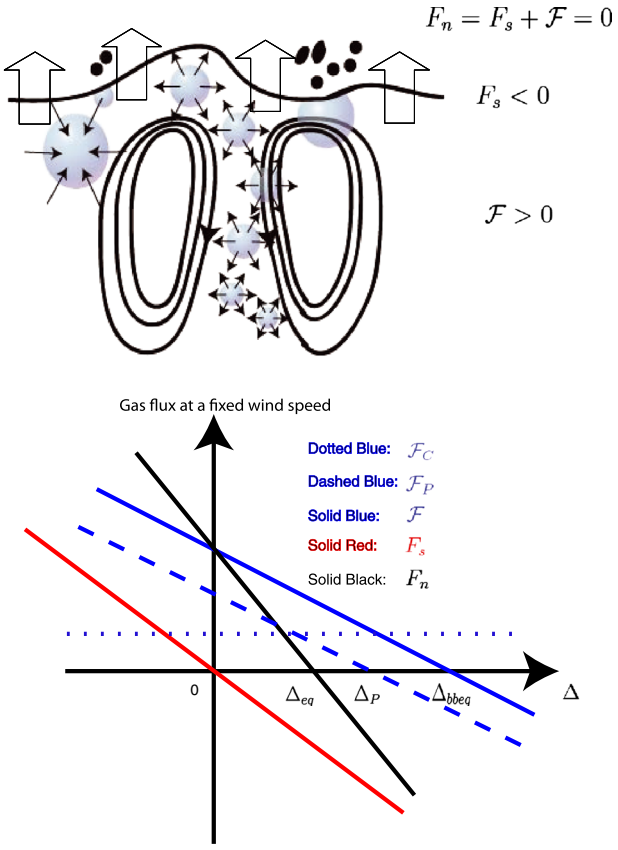

Figure 1. (top) An illustration of the mechanism of bubble-induced equilibrium supersaturation. (bottom) A schematic diagram showing relations between different parameters defined in equations (2), (3), and (8).

air-sea gas transfer in two ways. First, bubbles provide an additional air-water interface for the transfer of gases, speeding the rate of equilibration. We refer to this as the "kinetic bubble effect." Second, as bubbles are compressed by hydrostatic pressure and surface tension, gases inside can be squeezed into the surrounding seawater even when it is supersaturated with respect to the atmosphere, causing gases to diffuse from the ocean to the atmosphere through the air-sea interface. We refer to this as the "equilibrium bubble effect." The combined effect of bubbles on air-sea gas transfer are the enhancement of air-sea gas transfer rate and the elevation of the saturation state at which the dissolved gases are in equilibrium with the atmosphere.

[4] In this study, we derive a parameterization using bubble fields at different wind speeds. The bubble fields are calculated using a multisize multigas bubble model embedded in a large-eddy simulation model for oceanic boundary layer including wave effects [*Liang et al.*, 2011, 2012], which successfully simulates subsurface bubble evolution in turbulent oceanic boundary layers. This new parameterization, which is described in section 2, is compared with other published parameterizations [*Woolf and Thorpe*, 1991; *McNeil and D'Asaro*, 2007; *Stanley et al.*, 2009; *Vagle et al.*, 2010; *Ito et al.*, 2011; *Nicholson et al.*, 2011] in section 3. We then use a global transport model to evaluate the importance of bubble-induced equilibrium supersaturation level for deep ocean ventilation. A summary and outlook is given in section 5.

2. A Physically Based Parameterization for Air-Sea Gas Transfer

2.1. Basic Formulae

[5] The conventional view of air-sea gas transfer, in the absence of bubbles, is that gases go in and out of the ocean through diffusion across the air-sea interface. The net gas flux F_n is the gas flux through the ocean surface F_s and is parameterized as

$$F_n = F_s = K_s C_{\text{sat}} \left(\frac{P_{\text{slp}}}{P_{\text{atm}}} - \sigma \right), \tag{1}$$

where $C_{\text{sat}} = S\chi_{\text{atm}} P_{\text{atm}}$ is the saturation that would be in equilibrium with one standard atmospheric pressure (P_{atm}), with χ_{atm} the gas fraction in the atmosphere, and with S the temperature-dependent solubility [*Weiss*, 1970; *Hamme and Emerson*, 2004]. K_s is the gas transfer rate through ocean surface and is the only parameter in formula (1). P_{slp} is the local sea level pressure (SLP), and $\sigma = \frac{C}{C_{\text{sat}}}$ is the saturation level with C the concentration of a dissolved gas. The amount of dissolved gas will also be presented by its saturation anomaly as [e.g., *Emerson and Hedges*, 2008] $\Delta = \sigma - 100\%$.

[6] This common formulation of diffusive surface gas exchange (equation (1)) can be modified to include both the equilibrium and kinetic effects of bubbles in a simple way [e.g., *Woolf*, 1997],

$$F_n = K_T C_{\text{sat}} \left[(1 + \Delta_{\text{eq}}) \frac{P_{\text{slp}}}{P_{\text{atm}}} - \sigma \right]. \tag{2}$$

Here K_T is the gas transfer rate through the ocean surface and bubbles and thus accounts for the kinetic effect of bubbles. The term Δ_{eq} accounts for the equilibrium bubble effect and represents the bubble-induced supersaturation at which there is no net gas flux between the ocean and the atmosphere in steady state. When there are no bubbles in the water, i.e., $K_T = K_s$ and $\Delta_{\text{eq}} = 0$, equation (2) reduces to equation (1).

[7] In most ocean models that include gas exchange, the equilibrium bubble effect is neglected, i.e., $\Delta_{\text{eq}} = 0$, while the kinetic effect is implicitly included in empirical estimates of K_T and its dependence on the 10 m wind speed u_{10}. The wind speed dependence of K_T has been investigated by laboratory measurements [e.g., *Liss and Merlivat*, 1986], deliberate tracer experiments in the open ocean [e.g., *Wanninkhof et al.*, 1997; *Nightingale et al.*, 2000; *Ho et al.*, 2006], and atmospheric micrometeorological measurements above the open ocean [e.g., *Fairall et al.*, 2000; *Edson et al.*, 2011]. It is now generally accepted that $K_T \propto u_{10}^2$ to u_{10}^3 [e.g., *Wanninkhof et al.*, 2009].

[8] The contribution of bubbles to gas exchange depends strongly on the bubble size, as large and small bubbles have qualitatively different fates. Large bubbles, with fast buoyant rising speeds, only partially dissolve before they eventually burst at the ocean surface. Small bubbles, with slow buoyant rising speeds, can be effectively trapped in the water, allowing the gas contents to completely dissolve [e.g., *Keeling*, 1993; *Zhang*, 2012]. In light of this distinction, the net gas

flux can then be formulated as [e.g., *McNeil and D'Asaro*, 2007; *Stanley et al.*, 2009]

$$F_n = F_s + \mathcal{F}_P + \mathcal{F}_C = K_s C_{\text{sat}} \left(\frac{P_{\text{slp}}}{P_{\text{atm}}} - \sigma \right) + K_b C_{\text{sat}} \left((1 + \Delta_P) \frac{P_{\text{slp}}}{P_{\text{atm}}} - \sigma \right) + \mathcal{F}_C, \quad (3)$$

where the first term on the right represents gas exchange by ocean surface, the second term $\mathcal{F}_P$ on the right represents gas through large bubbles that partially dissolve, K_b is the gas transfer rate through large bubbles, Δ_P is the supersaturation due to partially dissolved bubbles, and the third term $\mathcal{F}_C$ on the right represents gas flux through small bubbles that completely dissolve. Equations (3) is consistent with equation (2) if

$$K_T = K_b + K_s, \quad (4)$$

and

$$\Delta_{\text{eq}} = \frac{K_b C_{\text{sat}} \Delta_P \frac{P_{\text{slp}}}{P_{\text{atm}}} + \mathcal{F}_C}{K_T C_{\text{sat}} \frac{P_{\text{slp}}}{P_{\text{atm}}}}. \quad (5)$$

This expresses the equilibrium bubble effect in terms of all the fundamental parameters.

[9] A useful diagnostic expression of the impact of bubbles on the equilibrium gas supersaturation can be obtained from combining the two bubble terms,

$$\mathcal{F} = \mathcal{F}_P + \mathcal{F}_C = K_b C_{\text{sat}} \left((1 + \Delta_{\text{bbeq}}) \frac{P_{\text{slp}}}{P_{\text{atm}}} - \sigma \right), \quad (6)$$

where

$$\Delta_{\text{bbeq}} = \Delta_P + \frac{\mathcal{F}_C}{K_b C_{\text{sat}} \frac{P_{\text{slp}}}{P_{\text{atm}}}}. \quad (7)$$

Δ_{bbeq} represents the saturation anomaly level when there is no net gas flux through all bubbles ($\mathcal{F} = 0$). The combined gas flux through both the air-sea interface and bubbles can now be written using Δ_{bbeq} as a single effective overpressure from both small and large bubbles,

$$F_n = F_s + \mathcal{F} = K_s C_{\text{sat}} \left(\frac{P_{\text{slp}}}{P_{\text{atm}}} - \sigma \right) + K_b C_{\text{sat}} \left((1 + \Delta_{\text{bbeq}}) \frac{P_{\text{slp}}}{P_{\text{atm}}} - \sigma \right). \quad (8)$$

At this saturation anomaly level, gases added from small bubbles that completely dissolve ($\mathcal{F}_C < 0$) is balanced by gas evasion into large bubbles ($\mathcal{F}_P > 0$). Recall that when $\Delta = \Delta_{\text{eq}}$, there is no net gas flux through the ocean surface, i.e., $F_{\text{net}} = 0$. At this saturation anomaly level, gases evade through the ocean surface ($F_s > 0$), yet the net gas flux through all bubbles is dissolved ($\mathcal{F} < 0$). Therefore, $\Delta_{\text{bbeq}} > \Delta_{\text{eq}}$. The relationship between different variables is illustrated in the bottom panel of Figure 1.

2.2. Determination of Parameters

[10] The total air-sea gas flux can be separated into a surface flux F_s and a bubble flux $\mathcal{F}$, as shown in equation (8). The surface flux is determined by a single parameter (K_s), while three additional parameters (K_b, $\mathcal{F}_c$, and Δ_P) are needed to compute bubble-mediated fluxes ($\mathcal{F}$). The parameterization of surface gas flux is adopted from an existing model formula, allowing us to focus on a new model for the bubble-mediated component of exchange. These are discussed in the next two subsections, respectively.

2.2.1. Gas Transfer Through Ocean Surface

[11] In order to separate diffusive surface gas exchange from the bubble effects, we must use estimates of K_s that do not already include the influence of bubbles on the gas exchange rate. We use the surface gas flux parameterization for K_s in the NOAA-COAREG (National Oceanic and Atmospheric Administration Coupled Ocean-Atmosphere Response Experiment) gas transfer parameterization [*Fairall et al.*, 2003, 2011; *Hare et al.*, 2004]. The NOAA-COAREG algorithm is among the few gas flux parameterizations that explicitly separate K_s and K_b, with the former given by [e.g., *Fairall et al.*, 2011]

$$K_s = \frac{u_*}{r_{\text{wt}} + \alpha r_a}, \quad (9)$$

where u_* is the friction velocity, r_{wt} is the waterside resistance to the transfer due to molecular turbulent processes, α is the dimensionless solubility, and r_a is the atmosphere side resistance. r_{wt}, α, and r_a in equation (9) were estimated using formulas and parameters suggested by *Fairall et al.* [2011]. Surface gas transfer rate for other gases are estimated using the surface renewal theory by *Fairall et al.* [2011],

$$K_s^{\text{gas}} = K_s^{660} \left(\frac{Sc^{\text{gas}}}{660} \right)^{-1/2}, \quad (10)$$

where Sc the Schmidt number and 660 is the value of Sc^{CO_2} at 20°C.

2.2.2. Gas Flux Through Bubbles

[12] Gas flux through bubbles can be estimated directly using subsurface bubble distribution [e.g., *Woolf and Thorpe*, 1991] or inversely using dissolved gas measurements [e.g., *Stanley et al.*, 2009]. In this study, we take the former approach. The bubble distribution and associated gas fluxes are calculated using a large-eddy simulation (LES) model coupled to a bubble population model [*Liang et al.*, 2011, 2012]; the important results of which are briefly described here.

[13] The coupled model simulates the simultaneous evolution of oceanic boundary layer turbulence and bubbles of 17 sizes (35 μm to 1 cm) containing two gases (O_2 and N_2). In the model, waves were assumed in equilibrium with local winds, which vary in strength from 5–20 m/s. Bubbles are injected during wave breaking. Their spatial and size distributions are constrained by laboratory measurements [*Deane and Stokes*, 2002; *Melville et al.*, 2002]. The ocean is covered by breaking waves of different lengths [e.g., *Melville and Matusov*, 2002]. The spatial distribution of bubbles under these breaking waves was calculated using a stochastic breaking wave model [*Sullivan et al.*, 2004, 2007; *McWilliams et al.*, 2012], which predicts a white cap coverage consistent with observations by *Wu* [1988]. The total amount of injected air conforms to observations that 50% of the breaking wave energy is consumed to deposit bubbles into the water [*Lamarre and Melville*, 1991]. The energy flux from breaking waves is parameterized following *Terray et al.* [1996] and is proportional to u_*^3 for a given sea state.

[14] In a near-surface horizontal plane, bubbles are organized into downwind streaks by the surface convergent flows of Langmuir circulations (Figure 2 top panel). Below these streaks are bubble plumes penetrating to more than

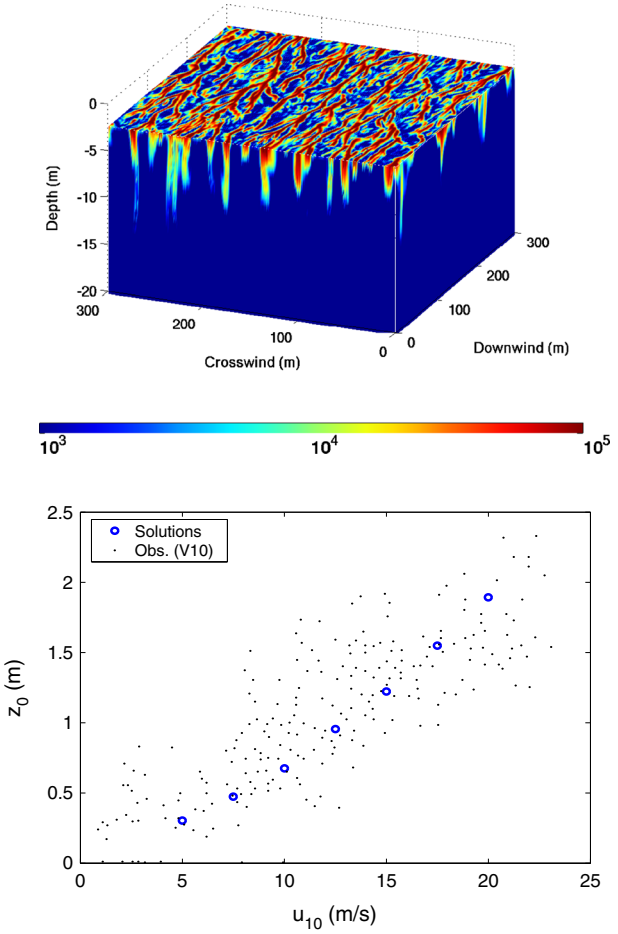

Figure 2. (top) An instantaneous snapshot of simulated total bubble number density (number per m^{-3}) at u_{10} = 17.5 m/s. (bottom) Relationship between bubble e-folding depth z_0 and wind speed u_{10}. (Black dots: observations by *Vagle et al.* [2010]; Blue circles: bubbly flow solutions assuming waves in equilibrium with local winds.)

10 m depth in the downward branches of Langmuir circulations. The near-surface streaks and intermittent bubble plumes have been observed in the ocean [*Farmer and Li*, 1995; *Vagle et al.*, 2010]. Although the spatial distribution of bubbles seem intermittent, the vertical distribution of total bubble number can be well described by an exponentially decaying function with depth, i.e., $\int C_b dr \propto \exp\left(\frac{z}{z_0}\right)$ with $C_b(r,z)$ the horizontally and temporally averaged bubble number density distribution and z_0 the bubble *e*-folding depth proportional to u_* for a given sea state. The oxygen fraction $\chi_b^{O_2}$ decreases with depth because O_2 dissolves faster than N_2. The numerical solutions have been validated against the few available observations [*Liang et al.*, 2011, 2012]. The bubble penetration depth in the model compares well with observations from the North Pacific by *Vagle et al.* [2010] (Figure 2 bottom panel). A more detailed description of the model and solutions and their validation against available observations can be found in *Liang et al.* [2011, 2012].

[15] To estimate the necessary bubble parameters from the model solutions, we must first estimate the gas fluxes and then use the results of section 2. Procedures for obtaining the three parameters are listed below:

[16] 1. *Compute gas flux from bubbles ($\mathcal{F}$).* Gas flux between bubbles and water at saturation level σ can be calculated from LES solutions using $C_b(r,z)$ and bubble gas fraction $\chi_b(r,z)$ as

$$\mathcal{F}(\sigma) = \int_{-\infty}^{0}\int_{0}^{\infty} \frac{dn}{dt}(r,z,\chi_b,\sigma) C_b(r,z) dr dz, \tag{11}$$

where $\frac{dn}{dt}(r,z,\chi_b,\sigma)$ is the gas flux between a bubble of radius r at a depth z containing χ_b fraction of the gas and water at saturation level σ and is calculated using parameters and formulas proposed by *Woolf and Thorpe* [1991] as $\frac{dn}{dt}(r,z,\chi_b,\sigma) \propto (Sc)^{-2/3} S\left(\chi_b \frac{P_b}{P_{atm}} - \sigma\right)$, with $P_b = P_{atm} - \rho g z + \frac{2\gamma}{r}$ the pressure exerted on the bubble and γ the surface tension coefficient.

[17] 2. *Estimate gas transfer rate through large bubbles (K_b).* Δ_{bbeq} is sought by equating $\mathcal{F}$ (formula (11)) to zero and noting that $\Delta = \sigma - 100\%$. According to equation (6), the gas transfer rate through bubbles K_b is then calculated by $K_b = \frac{\mathcal{F}(100\%)}{\Delta_{bbeq} C_{sat}}$. K_b for different gases can be scaled by $Sc^{-2/3}$, i.e., $K_b^{gas} = K_b^{660}\left(\frac{Sc^{gas}}{660}\right)^{-2/3}$.

[18] 3. *Compute gas flux by completely dissolved bubbles ($\mathcal{F}_C$).* The gas flux through completely dissolved bubbles is proportional only to gas fraction ($\mathcal{F}_C^{gas} \propto \chi_{atm}^{gas}$), while the gas flux through partially dissolved bubbles has additional Schmidt number and solubility dependence ($\mathcal{F}_P^{gas} \propto (Sc^{gas})^{-2/3}\chi_{atm}^{gas} S^{gas}$) [e.g., *Hamme and Emerson*, 2002; *Stanley et al.*, 2009]; $\mathcal{F}_C$ can be estimated as $\mathcal{F}_C = \frac{\mathcal{F}^{O_2}\chi_{atm}^{N_2} S^{N_2}(Sc^{N_2})^{-2/3} - \mathcal{F}^{N_2}\chi_{atm}^{O_2} S^{O_2}(Sc^{O_2})^{-2/3}}{\chi_{atm}^{O_2}\chi_{atm}^{N_2} S^{N_2}(Sc^{N_2})^{-2/3} - \chi_{atm}^{N_2}\chi_{atm}^{O_2} S^{O_2}(Sc^{O_2})^{-2/3}}$ with $\mathcal{F}_C^{gas} = \mathcal{F}_C \chi_{atm}^{gas}$.

[19] 4. *Estimate supersaturation by partially dissolved bubbles (Δ_P).* Having estimated the total gas flux and the flux from completely dissolved bubbles, the flux due to large bubbles can be computed by $\mathcal{F}_P = \mathcal{F} - \mathcal{F}_C$. According to equation (3), $\Delta_P = \frac{\mathcal{F}_P(100\%)}{K_b^{gas} C_{sat}^{gas}}$.

[20] Having extracted the bubble fluxes and the critical parameters (K_b, $\mathcal{F}_c$, and Δ_P) from the numerical solutions, we then relate them to meteorological conditions used to force the LES simulations. We plot each parameter against friction velocity u_* instead of the more commonly used u_{10}, because both injected bubble amount and bubble penetration depth depend directly on u_*. In this study, u_* is calculated as

$$u_* = \sqrt{\rho_a C_d/\rho_w}\, u_{10}, \tag{12}$$

where ρ_a is the atmosphere density, ρ_w is the ocean density, and C_d is the drag coefficient parameterized following *Large and Pond* [1981] with its value saturated at 20 m/s as suggested by *Sullivan et al.* [2012],

$$C_d = \begin{cases} 0.0012 & \text{if } |u_{10}| \le 11 \text{ m/s} \\ (0.49 + 0.0065|u_{10}|)\times 10^{-3} & \text{if } 11 \text{ m/s} < |u_{10}| < 20 \text{ m/s} \\ 0.0018 & \text{if } |u_{10}| \ge 20 \text{ m/s}. \end{cases} \tag{13}$$

Other formulas for u_* [e.g., *Fairall et al.*, 2011] could also be substituted into the parameterization formulas below.

[21] We assume a power-law relationship between each bubble-related parameter and the friction velocity from the

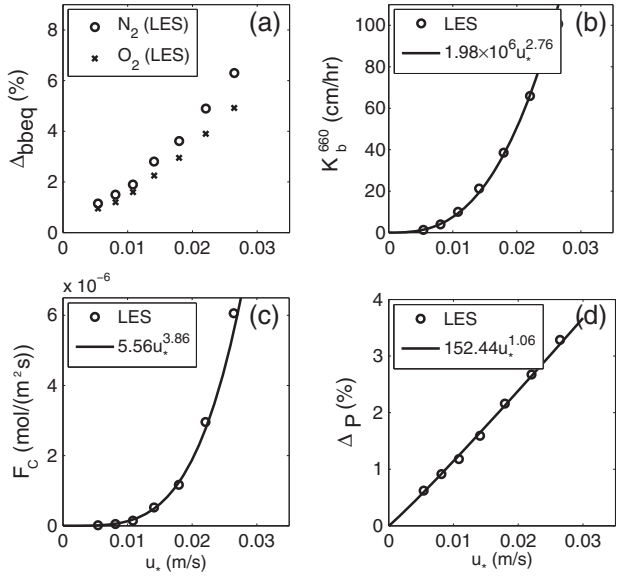

Figure 3. (a) Δ_{bbeq}: the saturation anomaly when the gas flux through all bubbles is zero, i.e., $\mathcal{F} = 0$), (b) K_b^{660} [cm/hr]: gas transfer rate through partially dissolved bubbles, (c) $\mathcal{F}_C$ [mol/(m^{2}s)]: gas transfer rate through partially dissolved bubbles, and (d) Δ_P: supersaturation due to partially dissolved bubbles derived from the bubble solutions calculated by the coupled LES—bubble population model. K_T, Δ_{bbeq}, $\mathcal{F}_C$, and Δ_P are defined in equations (2), (3), (8), and the texts below the equations. The open circles are from LES solutions at u_{10} = [5 : 2.5 : 20] m/s.

model simulations. By a least squares regression, we get (see Figure 3)

$$K_b^{\mathrm{gas}} = 1.98 \times 10^6 u_*^{2.76} \left(\frac{Sc^{\mathrm{gas}}}{660}\right)^{-2/3} \quad \mathrm{cm\ hr^{-1}}, \tag{14}$$

$$\mathcal{F}_C^{\mathrm{gas}} = \chi_{\mathrm{atm}}^{\mathrm{gas}} 5.56 u_*^{3.86} \quad \mathrm{mol\ s^{-1} m^{-2}}, \tag{15}$$

and

$$\Delta_P = 152.44 u_*^{1.06} \%. \tag{16}$$

[22] Equations (3), (9), (14), (15), and (16) complete the parameterization for the total air-sea gas flux including the effect of gas bubbles. From them, the bubble-induced supersaturation (Δ_{eq}) can be obtained following equation (5). Δ_{eq} increases with wind speeds (Figure 4). It is largest for least soluble gas (N_2) and is smallest for most soluble gas (CO_2). This is primarily because gas transfer through the ocean surface and partially dissolved bubbles is smaller for N_2 than for CO_2; the effect of completely dissolved bubbles is larger on $\Delta_{\mathrm{eq}}^{\mathrm{N_2}}$ than on $\Delta_{\mathrm{eq}}^{\mathrm{CO_2}}$, i.e., $\frac{\mathcal{F}}{K_T C_{\mathrm{sat}} \frac{P_{\mathrm{slp}}}{P_{\mathrm{atm}}}}$ in equation (5) is larger for N_2 than for CO_2 since N_2 is less soluble than CO_2.

[23] A less obvious characteristics of Δ_{eq} that has not been reported before is its temperature dependence. Δ_{eq} and T are inversely correlated (Figure 4). When temperature increases, $K_T C_{\mathrm{sat}}$ increases because the enhancement of K_T by decreasing Sc dominates the decrease in C_{sat} by decreasing solubility. Therefore, $\frac{\mathcal{F}_C}{K_T C_{\mathrm{sat}} \frac{P_{\mathrm{slp}}}{P_{\mathrm{atm}}}}$ is smaller, and Δ_{eq} is consequently smaller according to equation (5). Intuitively, turbulent diffusion and thus gas flux through both air-water interface and partially dissolved bubbles are larger at higher temperature, yet the gas flux through completely dissolved bubbles does not change with temperature. Therefore, the supersaturation needed to create the outgassing flux that balances dissolution through completely dissolved bubbles is smaller at a higher temperature. The temperature dependence is larger for less soluble gases (e.g., N_2) because the relative contribution from completely dissolved bubbles is larger for these gases. The temperature dependence of Δ_{eq} relies on the assumption that both bubble entrainment and penetration are independent of temperature. This assumption needs to be tested in the real ocean or laboratory. The uncertainties and caveats associated with this parameterization are detailed in the discussion section.

3. Comparisons With Other Parameterizations

[24] In this section, we compare the gas transfer parameterization derived in the previous section with five other existing air-sea gas transfer parameterizations including the effect of bubbles [*Fairall et al.*, 2011; *Woolf and Thorpe*, 1991; *Stanley et al.*, 2009; *Vagle et al.*, 2010; *Ito et al.*, 2011; *Nicholson et al.*, 2011] (Table 1). We included all available studies providing values for Δ_{eq}. For the ease of comparison, all parameterizations are converted to a common form as equation (2). The parameter dependencies for each model are summarized in Table 1, and a brief summary of qualitative features is given below.

[25] Parameterizations CW and L12 (this study) both directly derived Δ_{eq} from calculated bubble fields. Parameterization CW is in the form of equation (2). K_T is parameterized following NOAA-COAREG algorithm, with a gas transfer rate through the ocean surface using equation (9) and a gas transfer rate through bubbles proportional to ocean surface whitecap coverage, i.e., u_{10}^3 [e.g., *Asher et al.*, 1996; *Woolf*, 1997; *Monahan*, 2001; *Callaghan et al.*, 2008].

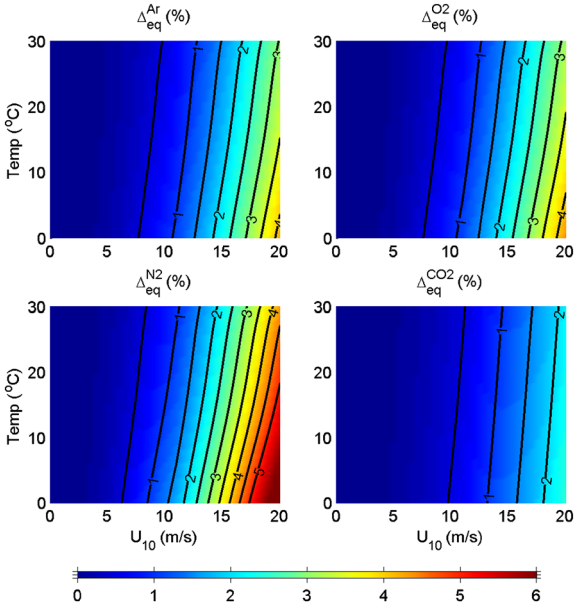

Figure 4. Wind speed and temperature dependence of Δ_{eq} (%) for four different gases (Ar, O_2, N_2, and CO_2).

Table 1. Air-Sea Gas Transfer Parameterizations Including Bubble Effect[a]

Abbreviation	Source	Parameters
CW (COAREG+WT91)	*Fairall et al.* [2011]; *Woolf and Thorpe* [1991]	$K_s \propto u_*$ $K_b \propto u_{10}^3$ $\Delta_{eq} \propto u_{10}^2$
S09	*Stanley et al.* [2009]	$K_s \propto u_{10}^2$ $K_b \propto u_{10}^3$ $\mathcal{F}_C \propto u_{10}^3$ $\Delta_P \propto u_{10}$
V10	*Vagle et al.* [2010]	$K_T \propto u_{10}^{2.62}$ $\mathcal{F}_C \propto u_{10}^{2.33}$
I11	*Ito et al.* [2011]	$K_T \propto u_{10}^2$ $\mathcal{F}_C \propto u_{10}^3$
N11	*Nicholson et al.* [2011]	$K_T \propto u_{10}^2$ $K_b\Delta_P \propto u_{10}^3$ $\mathcal{F}_C \propto u_{10}^3$
L12	This study	$K_s \propto u_*$ $K_b \propto u_*^{2.76}$ $\Delta_P \propto u_*^{1.06}$ $\mathcal{F}_C \propto u_*^{3.86}$

[a]Definition of parameters are in section 2.1. Detailed descriptions of the parameterizations are in sections 2.2 and 3.

The parameters used in this study are those tuned to radiocarbon observations [*Jeffery et al.*, 2010]. The NOAA-COAREG algorithm, which does not include a parameterization for Δ_{eq}, is combined with the Δ_{eq} parameterization by *Woolf and Thorpe* [1991], who fitted a u_{10}^2 dependence for Δ_{eq} using bubble fields calculated by an individual bubble model.

[26] The remaining parameterizations are based on dissolved gas observations. Parameterization S09 was proposed in the form of equation (3) [*Stanley et al.*, 2009]. It adopts the quadratic law by *Wanninkhof* [1992] for K_s. Δ_P is proportional to u_{10}. The magnitudes of $\mathcal{F}_C$ and K_b were tuned towards measured time series of upper ocean concentrations of five different inert gases (Ar, Kr, Xe, He, and Ne) at the Bermuda Atlantic Times-series Study (BATS) site. Parameterization V10 was proposed in the form of equation (3) but with $\Delta_P = 0$ [*McNeil and D'Asaro*, 2007; *Vagle et al.*, 2010]. K_T and $\mathcal{F}_C$ were obtained by a least squares fit to time series of near-surface-dissolved N_2 and O_2 concentration near Ocean Station Papa at the North Pacific Ocean. It uses an inverse algorithm developed by *McNeil and D'Asaro* [2007] whose parameters were based on hurricane winds and is thus not considered here. Parameterization I11 was proposed in the same form as V10 [*Ito et al.*, 2011], with magnitudes of K_T and $\mathcal{F}_C$ obtained by fitting a global mean surface Ne saturation level of 2%. Parameterization N11 was proposed in the form of equation (3) [*Nicholson et al.*, 2011], with parameter values determined by optimizing profiles of Ar, Ne, N_2/Ar, and Kr/Ar in a global transport model with observations at five different sites in the global ocean.

[27] The values for Δ_{eq} in parameterizations S09, V10, I11, and N11 were inferred from observations of Δ by removing the estimated contribution from heating/cooling, surface diffusive gas transfer, and mixing. An additional complication is that meteorological conditions other than wind speeds including wave age and surface heating/cooling modulate bubble distributions [*Woolf*, 2005; *Liang et al.*, 2012; *Vagle et al.*, 2012] and consequently Δ_{eq}. Parameterizations CW and L12 both directly derive Δ_{eq} from calculated bubble fields. In parameterization N11, N_2/Ar was used and this quantity is influenced by biogeochemical processes including denitrification [*DeVries et al.*, 2012] in addition to bubbles.

[28] All parameterizations predict similar trends and values for K_T^{660} (Figure 5a), and they are all within measured ranges [*Wanninkhof et al.*, 2009]. Other reported K_T^{660} [e.g., *Ho et al.*, 2006; *Wanninkhof et al.*, 2009; *Edson et al.*, 2011] span a wider range than shown in Figure 5a. They are not included in the comparison because they do not have a parameterization for Δ_{eq}. In contrast, the values for Δ_{eq} at a given temperature differ significantly among parameterizations.

[29] Values for $\Delta_{eq}^{CO_2}$ from S09, N11, and L12 are substantially larger than other parameterizations (Figure 5b). This is because these three parameterizations explicitly include the contributions from bubbles that partially dissolve, i.e., Δ_P, while the other three do not. The contribution from partially dissolved bubbles may be overestimated in these three parameterizations however, since they have not considered the possibility that CO_2 has equilibrated with the ambient water in intermediate-size bubbles while O_2 and N_2 have not (see section 5). $\Delta_{eq}^{CO_2} > 1\%$ at $u_{10} = 20$ m/s for S09 and L12. $\Delta_{eq}^{CO_2}$ in L12 increases faster with wind speed than in S09 and N11. In S09 and N11, the wind speed dependence of bubble-mediated gas flux is assumed the same as for whitecap coverage, i.e., proportional to u_{10}^3. However, recent

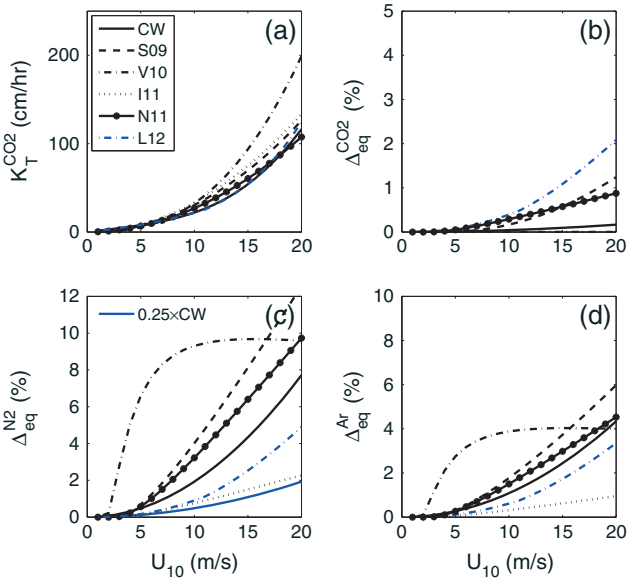

Figure 5. Wind speed dependence of (a) $K_T^{CO_2}$ (cm/hr), (b) $\Delta_{eq}^{CO_2}$ (%), (c) $\Delta_{eq}^{N_2}$ (%), and (d) Δ_{eq}^{Ar} (%) at 20°C using different parameterizations. K_T and Δ_{eq} are defined in equation (2) and the text below. $\frac{1}{4}$ of $\Delta_{eq}^{N_2}$ by *Woolf and Thorpe* [1991] is also plotted in Figure 5c because *Vagle et al.* [2010] found that model results agree better with their observations with the formula. Keys in the legend are explained in Table 1.

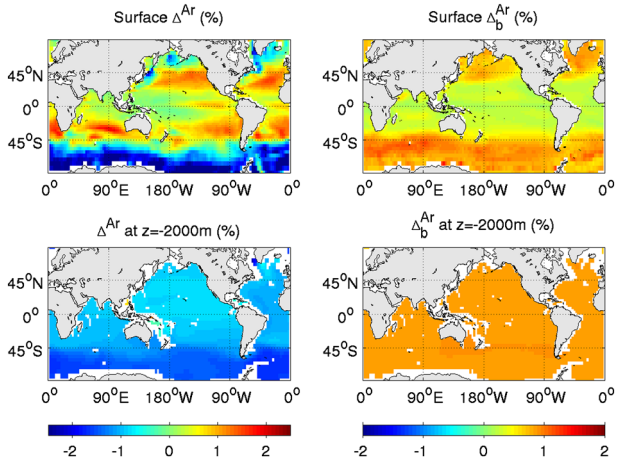

Figure 6. Maps of Δ^{Ar} (%) (left panels) and Δ_b^{Ar} (%) (right panels) at the surface and 2000 m depth.

studies [*McNeil and D'Asaro*, 2007; *Chiba and Baschek*, 2010; *Liang et al.*, 2012] show that the wind speed dependence of bubble-mediated gas flux is between u_{10}^5 and u_{10}^6 because both bubble injection and bubble penetration is a function of u_{10}.

[30] Figure 5c displays $\Delta_{eq}^{N_2}$ from different parameterizations. Besides the six parameterizations shown in Figures 5a and 5b, a line showing 0.25 of the $\Delta_{eq}^{N_2}$ in CW is added, as *Vagle et al.* [2010] reported that $0.25\times\Delta_{eq}^{N_2}$ in CW better reproduces their observations than the original formula in CW. $\Delta_{eq}^{N_2}$ is larger than $\Delta_{eq}^{CO_2}$ for the reason explained in section 2. The values for $\Delta_{eq}^{N_2}$ in different parameterizations also span a wide range. At u_{10} = 20 m/s, $\Delta_{eq}^{N_2}$ varies from about 2% (I11) to more than 12% (S09). Parameterization V10 predicts a distinctly different wind speed dependence for $\Delta_{eq}^{N_2}$, increasing sharply at low wind speed and leveling off at u_{10} > 8 m/s. This is because V10 did not prescribe the functional form of the wind speed dependence, in contrast to other gas-based models. Although values for $\Delta_{eq}^{N_2}$ from 0.25× CW, I11, and L12 are close at u_{10} < 10 m/s, their wind speed dependence is different among the three parameterizations. $\Delta_{eq}^{N_2}$ from L12 shows the strongest wind speed dependence. Parameterizations for Δ_{eq}^{Ar} show similar behavior as for $\Delta_{eq}^{N_2}$, except that values for Δ_{eq}^{Ar} are smaller than for $\Delta_{eq}^{N_2}$ (Figures 5d) because argon is slightly more soluble than nitrogen. The value for $\Delta_{eq}^{O_2}$ is similar to the value for Δ_{eq}^{Ar} and is not shown here. The ratio of Δ_{eq} between relatively insoluble gases (Ar and N_2) and soluble gas (CO_2) is larger in parameterization S09 than in parameterization L12. In parameterization S09 [*Stanley et al.*, 2009], more than 95% of the gas flux through bubbles comes from completely dissolved bubbles for relatively insoluble gases. In parameterization L12, the respective contributions from completely dissolved bubbles and from partially dissolved bubbles are comparable for relatively insoluble gases, as observed by *Hamme and Emerson* [2006].

[31] The temperature dependence reported in section 2 exists in all parameterizations listed in Table 1 except parameterization CW (not shown). Parameterization CW does not predict a temperature dependence for Δ_{eq} because it specifies a wind speed only dependence for Δ_{eq}.

4. Importance in Ocean Ventilation

[32] In this section, we assess the importance of bubble-induced equilibrium supersaturation state (Δ_{eq}) in ocean ventilation using a global transport model. We illustrate the role of bubbles using the inert gas argon because it is subject only to physical processes, including heating/cooling, mixing, and bubble processes, but has similar chemical properties to O_2. Argon has been commonly used to separate the contribution of physical processes on the saturation state of biogeochemically important gases, such as O_2 and N_2. For example, O_2 to Ar ratio has been used to quantify production/respiration [e.g., *Hamme et al.*, 2012], and N_2 to Ar ratio has been used to quantify denitrification [e.g., *Devola et al.*, 2006; *DeVries et al.*, 2012]. The bubble effects are also presented for biologically active gases, O_2, N_2, and CO_2, based on simulations without biological sources and sinks.

[33] The steady state concentrations of a tracer ($\vec{c}$) in the global ocean are calculated using the transport matrix method [*Khatiwala et al.*, 2005; *Khatiwala*, 2008]. This approach is much faster than a full general circulation model run and allows us to test different parameterizations in a short time. The model solves the equation

$$\vec{A}\vec{c} = \frac{\vec{F}}{\delta z_0}, \tag{17}$$

where $\vec{A}$ is the transport matrix representing the advection and diffusion of a tracer with concentration $\vec{c}$,$\vec{F}$ is the air-sea gas flux of the tracer, and δz_0 is the thickness of surface grid cell. In this study, $\vec{A}$ was derived from a solution of the Massachusetts Institute of Technology general circulation model (MITgcm) [*Marshall et al.*, 1997; *Khatiwala et al.*, 2005] that was configured with a horizontal resolution of 2.8° and 15 surface-intensified levels with the first level at 25 m depth.

[34] Air-sea gas flux parameters were calculated using daily climatological ocean surface conditions. The calculated daily gas fluxes were then averaged over a year. Sea level pressure originated from the National Centers for Environmental Prediction reanalysis [*Kanamitsu et al.*, 2002], and surface wind speeds were derived from QuikSCAT scatterometer wind (http://podaac.jpl.nasa.gov/OceanWind/QuikSCAT). The calculated gas flux was then multiplied by the ice-free fraction from Ocean Carbon-cycle Model Intercomparison Project Phase 2. Because the wind speed dependence of the air-sea gas flux is nonlinear, the use of wind speeds of lower temporal frequencies will yield smaller-averaged air-sea gas flux [*Sarmiento and Gruber*, 2006], i.e., $\left(\frac{1}{t_2-t_1}\int_{t_1}^{t_2} u_{10}\mathrm{d}t\right)^n < \frac{1}{t_2-t_1}\int_{t_1}^{t_2} u_{10}^n \mathrm{d}t$ when $n > 1$.

[35] We performed two sets of experiments. The first set of experiments are taken as control runs. In these experiments, parameterizations for both K_T and Δ_{eq} described in the previous section are used. The second set of experiments are designed to represent existing climate simulations, in which only the parameterization for K_T is used and Δ_{eq} is set to zero, i.e., F_n is calculated by equation (2) with Δ_{eq} = 0. This set of experiments mimics typical climate models by neglecting the equilibrium bubble effect and will be denoted as "No Δ_{eq} run" in the rest of the paper. The difference between the two sets of experiments is the supersaturation

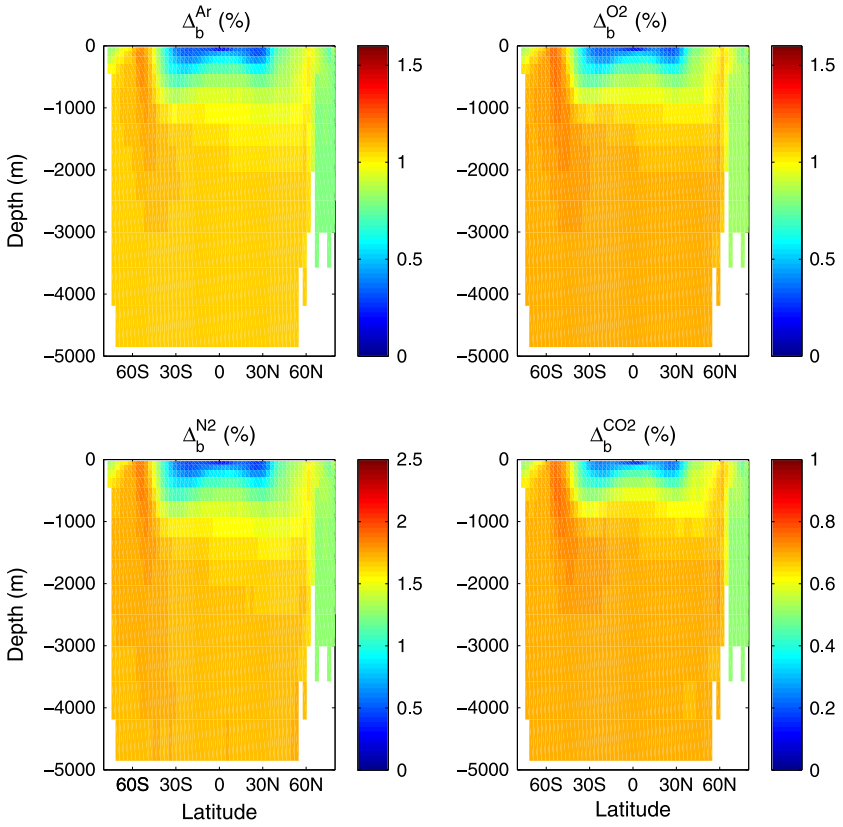

Figure 7. Zonally averaged vertical profiles of Δ_b^{Ar} (%) for four different gases (Ar, O_2, N_2, and CO_2).

state caused solely by bubble-induced supersaturation state Δ_b, i.e.,

$$\Delta_b = [\Delta]_{\text{controlrun}} - [\Delta]_{\text{no}\Delta_{\text{eq}}\text{run}}. \quad (18)$$

The geographic distribution of Δ^{Ar} in runs forced by L12 is shown in Figures 6 and 7. Gas fluxes calculated by other parameterizations yield similar patterns, although the values are different (not shown).

[36] Besides the two sets of experiments, an experiment with fast gas exchange is used to calculate the mixing induced supersaturation Δ_{mix} [*Ito et al.*, 2011]. In this experiment, SLP is set everywhere with one standard atmospheric pressure and K_T is set to a large value. The surface ocean is therefore everywhere 100% saturated, and any interior supersaturation is consequently caused only by mixing.

[37] Surface-dissolved argon is more than 2% undersaturated at high latitudes (poleward of 60° in both hemispheres), indicating oceanic uptake of Ar. At the eastern side of the basin at low latitude and midlatitude and at the tropics, near-surface Δ^{Ar} is positive and outgassing occurs. Ingassing at high latitudes and outgassing at low latitudes and midlatitudes are consistent with the oceanic cycle of other dissolved gases such as CO_2 [*Toggweiler et al.*, 2003]. The undersaturation at high latitudes and supersaturation at low latitudes is driven by cooling and warming, respectively, while air-sea gas fluxes reduce the latitudinal saturation contrast. Higher/lower gas transfer rate (larger/smaller K_T) leads to smaller/larger latitudinal saturation contrast. In the abyss (2000 m depth), the ocean is more than 1% undersaturated. The deep saturation anomaly is much more spatially uniform than near the surface.

[38] The bubble effect (Δ_b^{Ar}) is everywhere larger than zero at both the ocean surface and the ocean interior. At the ocean surface, Δ_b^{Ar} is more than 1% supersaturated at the southern ocean where the cooling-driven undersaturation is also high. Both the high wind speed and low temperature in this region are favorable for the equilibrium bubble effect (large Δ_{eq}^{Ar}) and, therefore, drive larger Δ_b^{Ar} than at the low-latitude and midlatitude surface ocean. Surface Δ_b^{Ar} at high latitudes of the North Atlantic and the North Pacific are slightly smaller than at the Southern Ocean but is also higher than at the low latitudes and midlatitudes. Δ_b^{Ar} in the ocean interior is much more spatially uniform than at the surface and is close to Δ_b^{Ar} of Southern Ocean surface.

[39] The processes underlying deep ocean saturation levels can be understood by examining meridional cross sections of gas saturation states (Figure 7). South of 45°S, Antarctic Bottom Water and Antarctic Intermediate water transport positive Δ_b^{Ar} north to the deep water of all three basins. In the Northern Hemisphere, North Atlantic Deep Water also transports positive Δ_b^{Ar} into the deep ocean, while the North Pacific Intermediate Water subducts positive Δ_b^{Ar} to between 1000 and 2000 m depth. The zonally averaged Δ_b for three other gases (O_2, N_2, and CO_2) exhibit similar spatial patterns to Ar but with different magnitudes (Figure 7). $\Delta_b^{CO_2}$ is possibly overestimated since the parameterization has not considered the possibility that CO_2 in partially dissolved bubbles equilibrate with ambient water. For a given wind speed, Δ_{eq} is largest for N_2 and smallest for CO_2; therefore, Δ_b is largest for N_2 and smallest for CO_2.

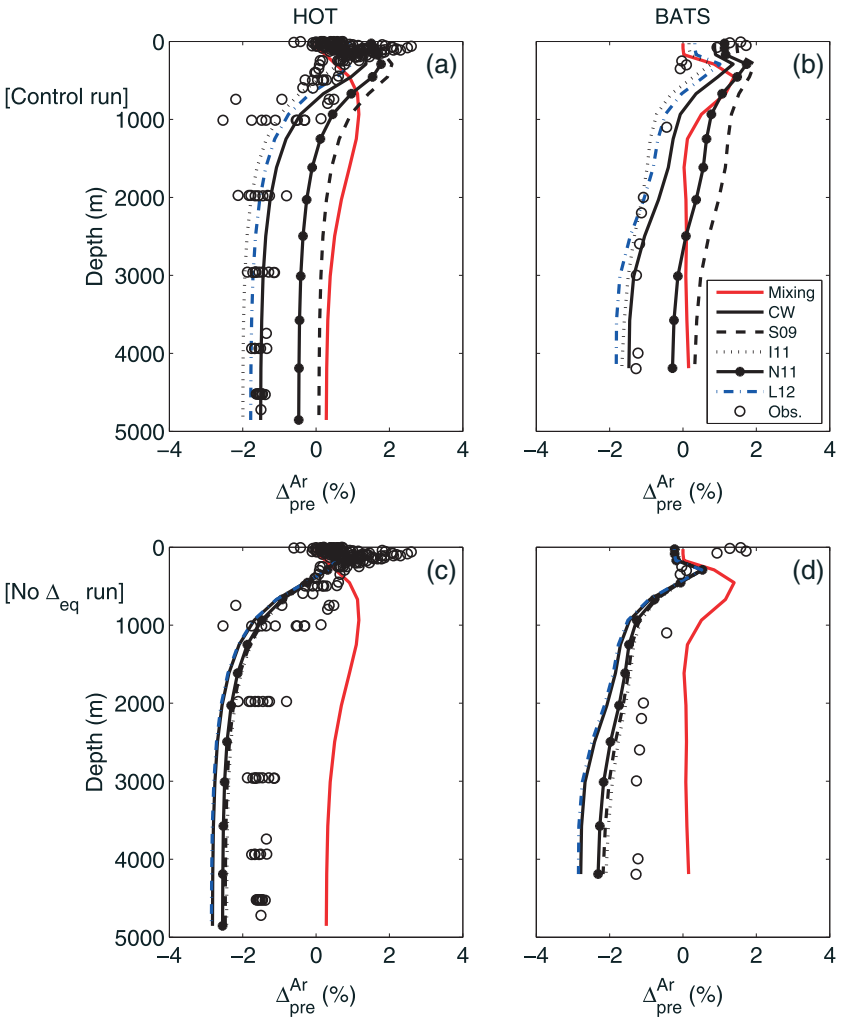

Figure 8. Profiles of Δ^{Ar}_{pre} and Δ^{Ar}_{mix} (%) at the Hawaiian Ocean Time-series (HOT) site (left panels) and at the Bermuda Atlantic Time-series Study (BATS) site (right panels). Top panels are results from the control runs, and bottom panels are results from the no Δ_{eq} runs. The solution using parameterization V10 is not presented, as its prediction is strongly influenced by the large Δ_{eq} at low wind speeds (see Figure 5). Observations were obtained by *Hamme and Emerson* [2002]. Keys in the legend are explained in Table 1.

[40] The importance of bubbles for the saturation state of the deep ocean can be evaluated by comparing predictions from gas exchange models to inert gas observations. Observed profiles of argon from the Hawaii Ocean Time-series (HOT) site in the Pacific Ocean and the Bermuda Atlantic Time-series Study (BATS) site in the Atlantic Ocean provide a measure of the vertical and basin-scale Ar concentration gradients.

[41] To compare model-simulated saturation states to observations, we first subtract the supersaturation that arises due to mixing of gases with nonlinear thermal solubilities across oceanic temperature gradients [*Ito and Deutsch*, 2006]. These mixing effects are exaggerated by spurious numerical diffusion in coarse circulation models. Following *Ito and Deutsch* [2006], Δ^{Ar} can be separated into a preformed component Δ^{Ar}_{pre} and a mixing component Δ^{Ar}_{mix}, i.e., $\Delta^{Ar} = \Delta^{Ar}_{pre} + \Delta^{Ar}_{mix}$. Δ^{Ar}_{pre} is the combined consequence of surface gas exchange processes including bubble-induced supersaturation states (Δ_{eq}) and the heating/cooling during the transit of surface water into the deep ocean. It is calculated by subtracting Δ_{mix} estimated in the run with fast gas exchange from Δ in the control run and the no Δ_{eq} run.

[42] Argon concentrations at different depths reflect surface processes at different locations and physical process during their transit in the ocean. In the control runs, Δ^{Ar}_{pre} decreases with water depth; however, the deep ocean Δ^{Ar}_{pre} span a wide range among parameterizations (Figures 8a and 8b). Parameterizations S09 and N11 predict larger values than observations at both sites. Modeled abyssal Δ^{Ar}_{pre} using the other three parameterizations (CW, I11, and L12) are close to observed values at both sites. Figures 8c and 8d compare modeled Δ^{Ar}_{pre} profile from the no Δ_{eq} runs with observations. Difference in the results in these runs arises from the difference in K_T. Faster/slower gas transfer (larger/smaller K_T) offsets more/less cooling-driven undersaturation at high-latitude surface ocean and predicts smaller/larger undersaturation in the abyss. Calculated no Δ_{eq} run profiles have similar shapes as in the control runs (Figures 8a and 8b). Results using different parameterizations differ much less than in the control runs, primarily

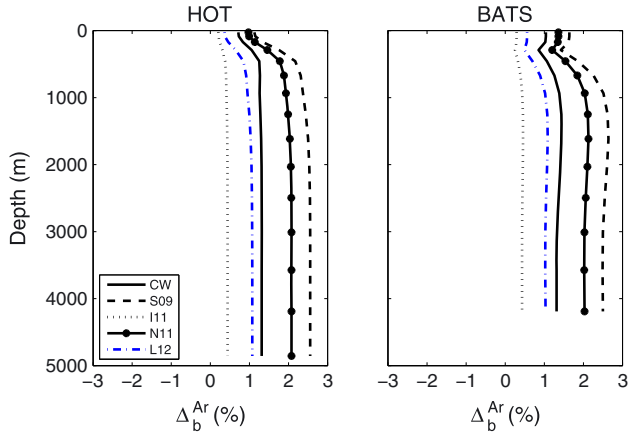

Figure 9. Profiles of Δ_b^{Ar} (%) at the two sites. Keys in the legend are explained in Table 1.

because the values for K_T in all the parameterizations are similar. The similar results among the no Δ_{eq} runs imply that the difference shown in modeled Δ_{pre}^{Ar} in the control runs mainly comes from the difference of Δ_{eq}^{Ar} in different parameterization schemes. As mentioned in section 3, observed K_T has a larger variability than the parameterizations chosen here. All runs using parameterizations excluding the effect of bubble-induced equilibrium supersaturation underestimate observed Δ^{Ar}.

[43] Figure 9 shows the profiles of Δ_b^{Ar} at both sites. The values of Δ_b^{Ar} are higher at depth than near surface, because Δ_b^{Ar} at depth originates from surface Δ_b^{Ar} at high latitudes where wind speeds are higher and temperatures are lower than at the surface of both sites. Δ_b^{Ar} is the primary cause of the difference of Δ_{pre}^{Ar} and consequently the difference of Δ_b^{Ar} between different parameterizations. The abyssal Δ_b^{Ar} is between 0.4% (I11) and 2.6% (S09) at the HOT site and between 0.4% and 2.5% at the BATS site.

[44] Model runs shown above are driven by annual mean transport matrix. The abyssal Δ^{Ar} is controlled by surface Δ^{Ar} at high latitudes where deep waters form. Deep waters preferentially form in winter [*Marshall and Schott*, 1999] when the oceanic temperature is lower, the wind speed is higher, and the sea ice coverage is higher than in other seasons. The different winter time conditions have different impact on high-latitude surface and abyssal saturation levels. Lower temperature drives larger undersaturation. Both the slower gas transfer under lower temperature (the effect of convection which possibly enhances gas transfer rate [e.g., *Rutgersson et al.*, 2011] is neglected in all the parameterizations used in this study) and the smaller gas flux due to higher ice coverage further drive larger undersaturation. However, lower temperature implies larger bubble-induced surface equilibrium supersaturation (Δ_{eq}) and reduces undersaturation. Higher wind speed also reduces undersaturation by driving faster gas transfer and larger bubble effect. The combined effect of all these conditions deserves further study in the future.

5. Discussion and Outlook

[45] Our results provide a first-order estimate of bubble-induced equilibrium saturation state and its effect in the global ocean by relating gas flux through bubbles to wind speed and using an ocean circulation model to propagate saturation level set by these fluxes into the ocean interior. Important uncertainties remain, however, both in the parameterization of the small-scale process of bubble-induced gas exchange and in the large-scale representation of the physical processes that carry the bubble signature to depth. Here we summarize the results of the preceding sections, discuss the caveats that arise from this work, and offer suggestions for future refinements.

[46] We derived a parameterization for bubble-mediated gas transfer based on size-resolved bubble fields at different wind speeds calculated by a model of the turbulent oceanic boundary layer. The fluxes due to small collapsing bubbles and large partially dissolving bubbles are considered separately. Gas flux through bubbles is regressed against friction velocity which governs both bubble injection and bubble penetration depth. Bubble-induced surface equilibrium supersaturation rises rapidly with wind speed and is shown to be inversely related to temperature. These combined effects yield bubble-induced equilibrium supersaturation that is higher at high latitudes, offsetting the undersaturations that arise from surface cooling. The magnitude of this effect varies widely, however, among the different published parameterizations for the effect of bubbles. This uncertainty stems from the wide range of predictions for the wind speed dependence of bubble fluxes and their parameters.

[47] There are three primary uncertainties associated with our estimates of bubble-induced ocean ventilation. First, gas flux through bubbles ($\mathcal{F}$) is determined by both bubble penetration and bubble entrainment. In the bubbly flow solutions used here, bubble penetration depth is controlled by ocean turbulence, while the absolute bubble amount is determined by bubble injection rate. Bubble injection rates applied here have been tuned to best match a series of laboratory and in situ measurements (see section 2). Nevertheless, uncertainties in bubble injection rate will lead to uncertainty in the resulting formulas (14) and (16). We are unable to quantitatively estimate the uncertainty in the measurements we fitted to and therefore the bubble injection rate used in the model. Both K_b and $\mathcal{F}_C$ change proportionally with bubble injection rate, while Δ_P is controlled by bubble penetration and do not change with bubble injection rate.

[48] Only the wind speed dependence of Δ_{eq} is considered in this study. Recent studies have suggested that meteorological conditions besides wind speed, such as sea state and buoyancy flux, are additional governing factors for bubble injection and penetration [*Woolf*, 2005; *Liang et al.*, 2012; *Vagle et al.*, 2012]. These factors will also contribute to the variability of gas flux through bubbles and may be particularly important at high latitudes where turbulence is primarily driven by surface cooling.

[49] Second, our parameterization is based on simulations that include only N_2 and O_2. It should therefore be considered accurate for gases with solubility similar to or less than those gases (e.g., Ar discussed extensively in section 4). However, the formulation may overestimate Δ_{eq} for highly soluble gases such as CO_2. For bubbles that are small enough to have a relatively long life yet large enough to eventually burst at the ocean surface rather than completely collapsing, highly soluble gases may have equilibrated with

the surrounding water [*Keeling*, 1993; *Woolf*, 1993, 1997], while the less soluble but abundant gases (N_2 and O_2) have not. Addressing this possibility will require additional LES simulations that explicitly solve for CO_2 dissolution.

[50] Finally, accurate determination of abyssal Δ_b requires accurate representation of surface ocean conditions, especially at high latitudes during winter season where deep waters form. The use of circulation fields and meteorological conditions with variability at seasonal to synoptic scales is expected to provide a better estimate of bubble effect in the abyssal-dissolved gas concentration. Surface and circulation variability at interannual and longer time scales is also likely to be significant in abyssal gas concentrations.

[51] Advancement in these directions will require collaborative efforts from both observational and computational oceanographers. On the observation side, concurrent observations of subsurface bubbles populations, concentrations for multiple gases of different solubility, and ocean surface meteorological conditions have not been reported and can greatly improve our quantification of gas fluxes through bubbles. On the modeling side, the inclusion of highly soluble gases such as CO_2 will allow a more robust estimate of bubble effects on these gases. Explicit simulation of the ventilation processes, including subduction and convection, over a wider range of meteorological conditions will be needed to identify the bubble effects that are obtained during the time periods of water mass formation.

[52] **Acknowledgments.** This study was supported by the Office of Naval Research through contract N00014-08-1-0597. Computations were performed on supercomputers Thresher and Trestles at the San Diego Supercomputing Center and Bluefire at the National Center for Atmospheric Research (NCAR). NCAR is sponsored by the National Science Foundation. Observed dissolved argon concentration was downloaded from http://web.uvic.ca/rhamme/download.html. We would like to thank David Woolf and an anonymous reviewer for their constructive comments and suggestions.

References

Asher, W. E., L. M. Karle, B. J. Higgins, P. J. Farley, E. C. Monahan, and I. S. Leifer (1996), The influence of bubble plumes on air-seawater gas transfer velocities, *J. Geophys. Res.*, *101*, 12,027–12,041.

Baschek, B. (2003), Air-sea gas exchange in tidal fronts, Ph.D. thesis, Univ. of Victoria, Victoria, B.C., Canada.

Callaghan, A., G. de Leeuw, L. Cohen, and C. D. O'Dowd (2008), Relationship of oceanic whitecap coverage to wind speed and wind history, *Geophys. Res. Lett.*, *35*, L23609, doi:10.1029/2008GL036165.

Chiba, D., and B. Baschek (2010), The effect of Langmuir cells on bubble dissolution and air-sea gas exchange, *J. Geophys. Res.*, *115*, C10046, doi:10.1029/2010JC006203.

D'Asaro, E., and C. McNeil (2007), Air-sea gas exchange at extreme wind speeds measured by autonomous oceanographic floats, *J. Mar. Syst.*, *66*, 92–109.

Deane, G. B., and M. D. Stokes (2002), Scale dependence of bubble creation mechanisms in breaking waves, *Nature*, *418*, 839–844.

Devola, A. H., A. G. Uhlenhoppa, S. W. A. Naqvib, J. A. Brandesc, D. A. Jayakumard, H. Naikb, S. Gaurine, L. A. Codispotif, and T. Yoshinarig (2006), Denitrification rates and excess nitrogen gas concentrations in the Arabian Sea oxygen deficient zone, *Deep-Sea Res. I*, *53*(9), 1533–1547.

DeVries, T., C. Deutsch, F. Primeau, B. X. Chang, and A. H. Devol (2012), Global rates of water-column denitrification derived from nitrogen gas measurements, *Nat. Geosci.*, *5*, 547–550, doi:10.1038/NGEO1515.

Edson, J. B., C. W. Fairall, L. Bariteau, C. J. Zappa, A. Cifuentes-Lorenzen, W. R. McGillis, S. Pezoa, J. E. Hare, and D. Helmig (2011), Direct covariance measurement of CO2 gas transfer velocity during the 2008 Southern Ocean Gas Exchange Experiment: Wind speed dependency, *J. Geophys. Res.*, *116*, C00F10, doi:10.1029/2011JC007022.

Emerson, S. R., and J. I. Hedges (2008), *Chemical Oceanography and the Marine Carbon Cycle*, Cambridge Univ. Press, Cambridge.

Fairall, C. W., J. E. Hare, J. B. Edson, and W. McGillis (2000), Parameterization and micrometeorological measurements of air-sea gas transfer, *Bound. Lay. Meteorol.*, *96*, 63–106, doi:10.1023/A:1002662826020.

Fairall, C. W., E. F. Bradley, J. E. Hare, A. A. Grachev, and J. B. Edson (2003), Bulk parameterization of air-sea fluxes: Updates and verification for the COARE algorithm, *J. Clim.*, *16*, 571–591.

Fairall, C. W., M. Yang, L. Bariteau, J. B. Edson, D. Helmig, W. McGillis, S. Pezoa, J. E. Hare, B. Huebert, and B. Blomquist (2011), Implementation of the coupled ocean-atmosphere response experiment flux algorithm with CO2, dimethyl sulfide, and O3, *J. Geophys. Res.*, *116*, C00F09, doi:10.1029/2010JC006884.

Farmer, D., and M. Li (1995), Patterns of bubble clouds organized by Langmuir circulation, *J. Phys. Oceanogr.*, *25*, 1426–1440.

Hamme, R. C., and S. R. Emerson (2002), Mechanisms controlling the global oceanic distribution of the inert gases argon, nitrogen and neon, *Geophys. Res. Lett.*, *29*(23), 2120, doi:10.1029/2002GL015273.

Hamme, R. C., and S. R. Emerson (2004), The solubility of neon, nitrogen and argon in distilled water and seawater, *Deep-Sea Res. I*, *51*, 1517–1528, doi:10.1016/j.dsr.2004.06.009.

Hamme, R. C., and S. R. Emerson (2006), Constraining bubble dynamics and mixing with dissolved gases: Implications for productivity measurements by oxygen mass balance, *J. Mar. Res.*, *64*, 73–95, doi:10.1357/002224006776412322.

Hamme, R. C., et al. (2012), Dissolved O2/Ar and other methods reveal rapid changes in productivity during a Lagrangian experiment in the Southern Ocean, *J. Geophys. Res.*, *117*, C00F12, doi:10.1029/2011JC007046.

Hare, J. E., C. W. Fairall, W. R. McGillis, J. B. Edson, B. Ward, and R. Wanninkhof (2004), Evaluation of the National Oceanic and Atmospheric Administration/Coupled-Ocean Atmospheric Response Experiment (NOAA/COARE) air-sea gas transfer parameterization using GasEx data, *J. Geophys. Res.*, *109*, C08S11, doi:10.1029/2003JC001831.

Ho, D. T., C. S. Law, M. J. Smith, P. Schlosser, M. Harvey, and P. Hill (2006), Measurements of air-sea gas exchange at high wind speeds in the Southern Ocean: Implications for global parameterizations, *Geophys. Res. Lett.*, *33*, L16611, doi:10.1029/2006GL026817.

Ito, T., and C. Deutsch (2006), Understanding the saturation state of argon in the thermocline: The role of air-sea gas exchange and diapycnal mixing, *Global Biogeochem. Cycles*, *20*, GB3019, doi:10.1029/2005GB002655.

Ito, T., C. Deutsch, S. Emerson, and R. C. Hamme (2007), Impact of diapycnal mixing on the saturation state of argon in the subtropical North Pacific, *Geophys. Res. Lett.*, *34*, L09602, doi:10.1029/2006GL029209.

Ito, T., R. C. Hamme, and S. Emerson (2011), Temporal and spatial variability of noble gas tracers in the North Pacific, *J. Geophys. Res.*, *116*, C08039, doi:10.1029/2010JC006828.

Jeffery, C. D., I. S. Robinson, and D. K. Woolf (2010), Tuning a physically based model of the air-sea gas transfer velocity, *Ocean Model.*, *31*, 28–35.

Jenkins, W. J. (1982), Oxygen utilization rates in North Atlantic subtropical gyre and primary production in oligotrophic systems, *Science*, *5889*, 246–248.

Kanamitsu, M., W. Ebisuzaki, J. Woollen, S.-K. Yang, J. J. Hnilo, M. Fiorine, and G. L. Potter (2002), NCEP-DOE AMIP-II reanalysis (R-2), *Bull. Am. Meteorol. Soc.*, *83*, 1631–1643.

Keeling, R. F. (1993), On the role of large bubbles in air-sea gas exchange and supersaturation in the ocean, *J. Mar. Res.*, *51*, 237–271.

Khatiwala, S. (2008), Fast spin up of ocean biogeochemical models using matrix-free Newton-Krylov, *Ocean Model.*, *23*, 121–129.

Khatiwala, S., M. Visbeck, and M. A. Cane (2005), Accelerated simulation of passive tracers in ocean circulation models, *Ocean Model.*, *9*, 51–69.

Lamarre, E., and W. K. Melville (1991), Air entrainment and dissipation in breaking waves, *Nature*, *351*, 469–472.

Large, W. G., and S. Pond (1981), Open ocean momentum flux measurements in moderate to strong winds, *J. Phys. Oceanogr.*, *11*, 324–336.

Liang, J.-H., J. C. McWilliams, P. P. Sullivan, and B. Baschek (2011), Modeling bubbles and dissolved gases in the ocean, *J. Geophys. Res.*, *116*, C03015, doi:10.1029/2010JC006579.

Liang, J.-H., J. C. McWilliams, P. P. Sullivan, and B. Baschek (2012), Large eddy simulation of the bubbly ocean: New insights on subsurface bubble distribution and bubble-mediated gas transfer, *J. Geophys. Res.*, *117*, C04002, doi:10.1029/2011JC007766.

Liss, P. S., and L. Merlivat (1986), Air-sea gas exchange rates: Introduction and synthesis, in *The Role of Air-Sea Exchange in Geochemical Cycling*, edited by P. Buat-Menard, pp. 113–129, MA: D. Reidel, Norwell.

Marshall, J., and F. Schott (1999), Open-ocean convection: Observations, theory and models, *Rev. Geophys.*, *37*, 1–46.

Marshall, J., A. Adcroft, C. Hill, L. Perelman, and C. Heisey (1997), A finite-volume, incompressible Navier Stokes model for studies of the

ocean on parallel computers, *J. Geophys. Res.*, *102*(C3), 5753–5766, doi:10.1029/96JC02775.

McNeil, C., and E. D'Asaro (2007), Parameterization of air-sea gas fluxes at extreme wind speeds, *J. Mar. Syst.*, *66*, 110–121.

McWilliams, J. C., E. Huckle, J.-H. Liang, and P. P. Sullivan (2012), The wavy Ekman layer: Langmuir circulations, breaking waves, and Reynolds stress, *J. Phys. Oceanogr.*, *42*, 1793–1816.

Melville, W. K., and P. Matusov (2002), Distribution of breaking waves at the ocean surface, *Nature*, *417*, 58–63.

Melville, W. K., F. Veron, and C. J. White (2002), The velocity field under breaking waves: Coherent structures and turbulence, *J. Fluid Mech.*, *454*, 203–233.

Monahan, E. C. (2001), Whitecaps and foam, in *Encyclopedia of Ocean Sciences*, edited by J. Steele, S. Thorpe, and K. Turekian, pp. 3213–3219, Academic Press, New York.

Nicholson, D., S. Emerson, N. Caillon, J. Jouzel, and R. C. Hamme (2010), Constraining ventilation during deepwater formation using deep ocean measurements of the dissolved gas ratios 40Ar/36Ar, N2/Ar, and Kr/Ar, *J. Geophys. Res.*, *115*, C11015, doi:10.1029/2010JC006152.

Nicholson, D. P., S. R. Emerson, S. Khatiwala, and R. C. Hamme (2011), An inverse approach to estimate bubble-mediated air-sea gas flux from inert gas measurements, paper presented at 6th International Symposium on Gas Transfer at Water Surfaces, Kyoto Univ. Press, pp. 223–237.

Nightingale, P. D., G. Malin, C. S. Law, A. J. Watson, P. S. Liss, M. J. Liddicoat, J. Boutin, and R. C. Upstill-Goddard (2000), In situ evaluation of air-sea gas exchange using novel conservative and volatile tracers, *Global Biogeochem. Cycles*, *14*, 373–387, doi:10.1029/1999GB900091.

Rutgersson, A. A., A. Smedman, and E. Sahlee (2011), Oceanic convective mixing and the impact on air-sea gas transfer velocity, *Geophys. Res. Lett.*, *38*, L02602, doi:10.1029/2010GL045581.

Sarmiento, J. L., and N. Gruber (2006), *Ocean Biogeochemical Dynamics*, Princeton Univ. Press, Princeton, N. J.

Stanley, R. H. R., W. J. Jenkins, D. E. Lott III, and S. C. Doney (2009), Noble gas constraints on air-sea gas exchange and bubble fluxes, *J. Geophys. Res.*, *114*, C11020, doi:10.1029/2009JC005396.

Sullivan, P. P., J. C. McWilliams, and W. K. Melville (2004), The oceanic boundary layer driven by wave breaking with stochastic variability. Part 1. Direct numerical simulations, *J. Fluid Mech.*, *507*, 143–174.

Sullivan, P. P., J. C. McWilliams, and W. K. Melville (2007), Surface gravity wave effects in the oceanic boundary layer: Large-eddy simulation with vortex force and stochastic breakers, *J. Fluid Mech.*, *593*, 405–452.

Sullivan, P. P., L. Romero, J. C. McWilliams, and W. K. Melville (2012), Transient evolution of Langmuir turbulence in ocean boundary layers driven by hurricane winds and waves, *J. Phys. Oceanogr.*, *42*, 1959–1980.

Terray, E. A., M. A. Donelan, Y. C. Agrawal, W. M. Drennan, K. K. Kahma, A. J. Williams III, P. A. Hwang, and S. A. Kitaigorodskii (1996), Estimates of kinetic energy dissipation under breaking waves, *J. Phys. Oceanogr.*, *26*, 792–807.

Toggweiler, J. R., A. Gnanadesikan, S. Carson, R. Murnane, and J. L. Sarmiento (2003), Representation of the carbon cycle in box models and GCMs: 1. Solubility pump, *Global Biogeochem. Cycles*, *17*(1), 1026, doi:10.1029/2001GB001401.

Vagle, S., C. McNeil, and N. Steiner (2010), Upper ocean bubble measurements from the NE pacific and estimates of their role in air-sea gas transfer of the weakly soluble gases nitrogen and oxygen, *J. Geophys. Res.*, *115*, C12054, doi:10.1029/2009JC005990.

Vagle, S., J. Gemmrich, and H. Czerski (2012), Reduced upper ocean turbulence and changes to bubble size distributions during large downward heat flux events, *J. Geophys. Res.*, *117*, C00H16, doi:10.1029/2011JC007308.

Vlahos, P., and E. C. Monahan (2009), A generalized model for the air-sea transfer of dimethyl sulfide at high wind speeds, *Geophys. Res. Lett.*, *36*, L21605, doi:10.1029/2009GL040695.

Wanninkhof, R. (1992), Relationship between wind speed and gas exchange over the ocean, *J. Geophys. Res.*, *97*(C5), 7373–7382, doi:10.1029/92JC00188.

Wanninkhof, R., et al. (1997), Gas exchange, dispersion, and biological productivity on the west florida shelf: Results from a Lagrangian tracer study, *Geophys. Res. Lett.*, *24*(14), 1767–1770.

Wanninkhof, R., W. E. Asher, D. T. Ho, C. Sweeney, and W. R. McGillis (2009), Advances in quantifying air-sea gas exchange and environmental forcing, *Annu. Rev. Mar. Sci.*, *1*, 213–244.

Weiss, R. F. (1970), The solubility of nitrogen, oxygen and argon in water and seawater, *Deep Sea Res.*, *17*, 721–735.

Woolf, D. K. (1993), Bubbles and the air-sea transfer velocity of gases, *Atmos. Ocean*, *31*(4), 517–540.

Woolf, D. K. (1997), Bubbles and their role in gas exchange, in *The Sea Surface and Global Change*, edited by P. S. Liss and R. A. Duce, pp. 173–205, Cambridge Univ. Press, Cambridge.

Woolf, D. K. (2005), Parametrization of gas transfer velocities and sea-state-dependent wave breaking, *Tellus B*, *57B*, 87–94.

Woolf, D. K., and S. A. Thorpe (1991), Bubbles and the air-sea exchange of gases in near-saturation conditions, *J. Mar. Res.*, *49*, 435–466.

Wu, J. (1988), Variations of whitecap coverage with wind stress and water temperature, *J. Phys. Oceanogr.*, *18*, 1448–1453.

Zhang, X. (2012), Contribution to the global air-sea CO2 exchange budget by asymmetric bubble-mediated gas transfer, *Tellus B*, *64*, 17,260.